RESEARCH ARTICLE

WILEY Journal of RAMAN SPECTROSCOPY

Hyper-spectral Raman imaging correlating chemical substitution and crystallinity in biogenic hydroxyapatite: Dentin and enamel in normal and hypoplastic human teeth

Ping Wang[1] | Evan J.D. Anderson[2] | Eric A. Muller[2] | Fuhua Gao[1] | Yisi Zhong[3,4] | Markus B. Raschke[2] (iD)

[1] Sichuan University, College of Physical Science and Technology, Chengdu, China

[2] University of Colorado at Boulder, Department of Physics, Department of Chemistry, and JILA, Boulder, Colorado, U.S.A.

[3] Sichuan University, West China School of Stomatology, Chengdu, China

[4] State Key Laboratory of Oral Diseases, Chengdu, China

Correspondence

Markus Raschke, Department of Physics, Department of Chemistry, and JILA, University of Colorado at Boulder, Boulder, CO 80309.
Email: markus.raschke@colorado.edu

Yisi Zhong, West China School of Stomatology, Sichuan University, Chengdu, China.
Email: zhongsissi@sina.com

Abstract

Micro-Raman imaging and spectroscopy has become an established technique for the characterization of biogenic hydroxyapatite as, for example, the primary constituent of human teeth. However, few studies have yet gone beyond a qualitative analysis of the Raman response providing only limited insight into spatial heterogeneity of composition, structure, and degree of crystallinity. Here, we show how correlative electron microprobe and extended hyperspectral Raman imaging with high spatial and spectral resolution, with peak position and linewidth analysis, and from the μm to mm scale, provides insight into structural characteristics in dentin and enamel. From comparison of healthy and hypoplastic teeth as a representative tooth disease example, we determine variations in degree of crystallinity, both locally across the dentin–enamel junction, and with distinct long-range spatial variations. We identify a correlation of spectral peak position and linewidth as a measure of crystal lattice disorder across tubules, dentin, dentin–enamel junction, and enamel. This correlative Raman imaging and analysis approach may help to provide a better understanding of apatite geochemistry and biomineralization.

KEYWORDS

hypoplastic tooth, micro-Raman imaging, structure correlation, tooth apatite

1 | INTRODUCTION

Micro-Raman spectroscopy and imaging has become an established analytical vibrational spectroscopic technique that is label-free, minimally invasive, and chemically specific. It has particular virtues for the study of biomineralization, being sensitive to both bio-organic material and inorganic mineral phases and their spatial distribution and relationship.[1]

A prime example is the application of Raman spectroscopy for the study of biogenic hydroxyapatite $Ca_{10}(PO_4)_6(OH)_{10}$ in bone, teeth, soft tissue, fossils, coprolite, and so forth. Notably, in its application to human teeth, Raman spectroscopy has found widespread use helping to understand structure and composition as related to enamel and dentin chemical resistance, mechanical properties, protein alteration, and tooth diseases.[2–8]

Micro-Raman imaging has been widely employed to identify the dentin–enamel junction (DEJ) separating the hard outer enamel from the soft inner dentin region.[9–12] Of particular interest has been the width of the DEJ, spatial variations within the dentin and enamel regions, and modifications associated to different tooth diseases.[13–15] In particular, to gain insight into structural

changes across the DEJ, spatial variations in lineshape of the phosphate Raman mode have been analyzed,[7,9,16,17] yet without the relationship of the Raman response to chemical and structural parameters of the apatite.

While recent advanced electron, X-ray, and other imaging techniques have identified many of the relationships of apatite crystallite size and orientation, lattice parameter, chemical substitution, and mechanical properties, in enamel and dentin,[18–23] the correlation of these properties with their corresponding Raman signature has not yet been systematically established. To establish the correlation of the Raman response with chemical and lattice structural parameters is particularly desirable for biogenic apatite, because Raman spectroscopy provides the complementary direct distinction of protein and other minor organic constituents, not readily identifiable by other techniques.

Here, we demonstrate an extended and systematic approach to full micro-Raman spatio-spectral imaging, with mapping of linewidth and spectral position of the ν_1 PO_4^{3-} P-O stretch mode as a probe of chemical substitution and associated lattice disorder. In the application to dentin and enamel in both normal and hypoplastic teeth, as an example for a tooth disorder, we show sensitivity with distinct both long and short range variations in degree of crystallinity. Further, we resolve correlated variations in spectral position, full width at half maxima (FWHM), and chemical substitution with characteristics specific for the main tooth phases of dentinal tubules (DT), intertubular dentin (ID), DEJ, enamel and correlated spatio-chemical variations, and crystallographic lattice parameter. This deeper level of microscopic insight provided by spatio-spectral Raman imaging might lead to improved diagnostics and treatments methods for tooth diseases and demonstrates the applicability of multimodal spatio-spectral imaging for studies of biomineralization in other systems.

2 | EXPERIMENT

2.1 | Sample preparation

Permanent third molar teeth from patients were extracted for dental health purposes with patient consent and used with all patient identifying information removed. Two kinds of teeth, normally mineralized and hypoplastic teeth, were collected from two people of similar age.

Hypoplastic type enamel is a form of amelogenesis imperfecta, which belongs to a surface defect of the tooth crown[24] and has become the focus of recent studies.[7,8,25–27] The main feature of the hypoplastic teeth is a much thinner enamel than in normal tooth, with lower degree of mineralization with higher organic content, lower degree of crystallinity with more carbonate/Mg content and smaller crystal size, and lower microhardness.

The extracted teeth were thoroughly cleaned with deionized water and then stored in 0.9% (w/V) NaCl solution. The dried teeth were then embedded in epoxy-resin and sectioned perpendicular to the enamel surface to about 1 mm in thickness using a diamond saw. Section surfaces were serially polished using 800, 2,000, and 5,000 grit silicon carbide paper, and 0.5-μm diamond polishing suspension on cloth as the final step. Samples were ultrasonicated in distilled water for 10 min, then dried, and again cleaned using methanol. Microscopic photos were taken using 10× and 100× objectives. The roughness of the polished teeth surfaces was characterized using atomic force microscope to about 50 and 150 nm for enamel and dentin (rms values), respectively, (for atomic force microscope images, see Figure S1).

2.2 | Backscattered electron (BSE) and energy dispersive X-ray (EDX)

For precharacterization, BSE imaging and qualitative EDX spectroscopy characterization of the tooth samples is performed on an electron microprobe (JEOL JXA-8600) with line scans across dentin and enamel to determine minor and major element variations.

2.3 | Raman spectroscopy

Raman microspectroscopy and microimaging is performed on two Raman spectrometer systems. One setup (HR Evo Nano, Horiba Jobin Yvon, f = 800 mm) based on a confocal Raman microscope, using 632.8 nm excitation, a 100× objective (NA = 0.7, focus size ≈1 μm diameter), with power on sample of about 8 mW. Spectra are acquired using a grating of 1,200 grooves/mm providing for a spectral resolution of 0.5 cm^{-1}. The phonon band of silicon at 520.7 cm^{-1} was used to calibrate the spectrometer.

For higher optical throughput spatio-spectral large area scanning, Raman imaging was performed on a home-built system optimized for sensitivity, based on an upright microscope, (Olympus BX10) with 50× objective (NA = 0.8), 632-nm HeNe laser, with 1 mW at sample focus, and a f = 500-mm imaging spectrograph (Princeton Instruments spectrometer Acton SP500, with PIXIS 100 liquid nitrogen cooled charge-coupled device camera, calibrated on multiple spectral lines using a He-lamp). All spectra are analyzed using Voigt lineshape fitting using commercial (Horiba) and self-developed computational imaging code.

3 | RESULTS

3.1 | Morphology characterization

Representative tooth section optical microscope and BSE images extending from dentin to enamel of the normal and hypoplastic tooth at occlusal position each are shown in Figure 1a–d for normal tooth and Figure 1e–h for hypoplastic tooth sample (for additional micrographs of cervical position, see Figure S2). The occlusal position indicates the cusp tip position where the preameloblasts first differentiate from inner enamel epithelia on the dentin surface (red Box 1 in Figure 1a,e), whereas the cervical position is the point where the inner and outer enamel epithelia fuse to form Hertwig's epithelial root sheath (red Box 2 in Figure 1a,e).[28] The main feature of the hypoplastic tooth is the underdeveloped and thin enamel (e and f) compared with normal tooth (a and b). Under higher magnification, the DT and enamel spindle can clearly be discerned (Figure 1c,g), with in general similar characteristics in both normal and hypoplatic tooth. Figure 1 (c) and (g), and (d) and (h) are zoomed in from the areas as indicated (red box) in Figure 1b,f, respectively. They reveal small (<1 µm) features associated with DT.

EDX transects are obtained from dentin to enamel as indicated in Figure 1d,h (red dotted line). We define the spatial coordinates in the horizontal image directions relative to the DEJ, which we set to zero, with negative and positive distances into the dentin and enamel region, respectively (Section 3.2 below).

3.2 | Element distribution and Raman spectra

Semiquantitative analysis of the EDX transects yields the relative change of the major elements calcium (Ca) and phosphorous (P; Figure 2a) and minor elements sodium (Na) and magnesium (Mg; Figure 2b). The higher amounts of Ca and P in enamel are due to the ≈96 wt% of mineral content in enamel compared with only ≈70 wt% in dentin. Although Ca and P are correlated, Mg and Na are anticorrelated. The results are largely similar between healthy and hypoplastic tooth samples within the uncertainties of the measurements, possibly with a slightly higher Mg content in hypoplastic enamel compared with normal tooth. The Ca/P ratio is shown as function of Mg/P in Figure 2c. The false color scale indicates the measurement position relative to the DEJ as indicated in Figure 1d,h. The dentin and enamel form distinct populations, similar for both tooth types, yet a slightly lower Mg/P ratio in hypoplastic enamel for similar Ca/P ratios. The elemental trends generally agree with the distributions found in previous studies.[8,18,29,30]

Figure 2d shows representative micro-Raman spectra acquired in the enamel and dentin regions. The main component of dental enamel is highly mineralized and ordered crystalline hydroxyapatite with carbonate impurity. Correspondingly, the spectra of enamel are dominated by the four principal Raman-active vibrational modes of PO_4^{3-}. The peak at 430 cm^{-1} represents the doubly degenerate ν_2 O-P-O bend, 590 cm^{-1} is the triply degenerate ν_4 O-P-O bend, the dominant peak at 960 cm^{-1} is the totally symmetric ν_1 P-O band stretch, and 1,045 cm^{-1} is the asymmetric ν_3 P-O stretch.[1,31] In addition to phosphate, the symmetric stretch of the carbonate ion at 1,071 cm^{-1} can be identified spectrally overlapping with the 1,045 cm^{-1} phosphate stretch. The hydroxyapatite spectral response is in general similar between dentin and enamel, yet lower in intensity in dentin because of its greater organic content primarily in the form of Type I collagen.[28] The dentin exhibits additional peaks associated with the protein content at 1,245/1,271, 1,451, and 1,667 cm^{-1}, identified as amide III doublet, methylene deformation, and amide I stretch, respectively. The strong band around 2,940 cm^{-1} represents the symmetric stretch of the methylene group. The relative differences in peak intensities between dentin and enamel closely agree with previously reported spectra.[2,3,8]

FIGURE 1 Representative optical microscope images of the normal (a–c) and hypoplastic (e–g) teeth at increasing magnification. Backscattered electron image at the occlusal position of normal (d) and hypoplastic teeth (h) at the same locations shown in optical microscope images (c) and (g), respectively [Colour figure can be viewed at wileyonlinelibrary. com]
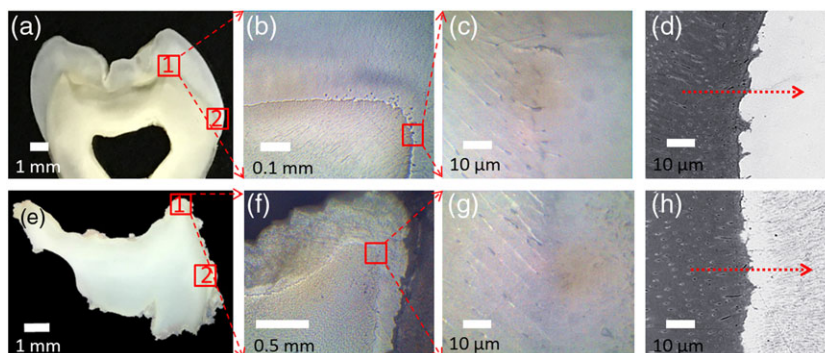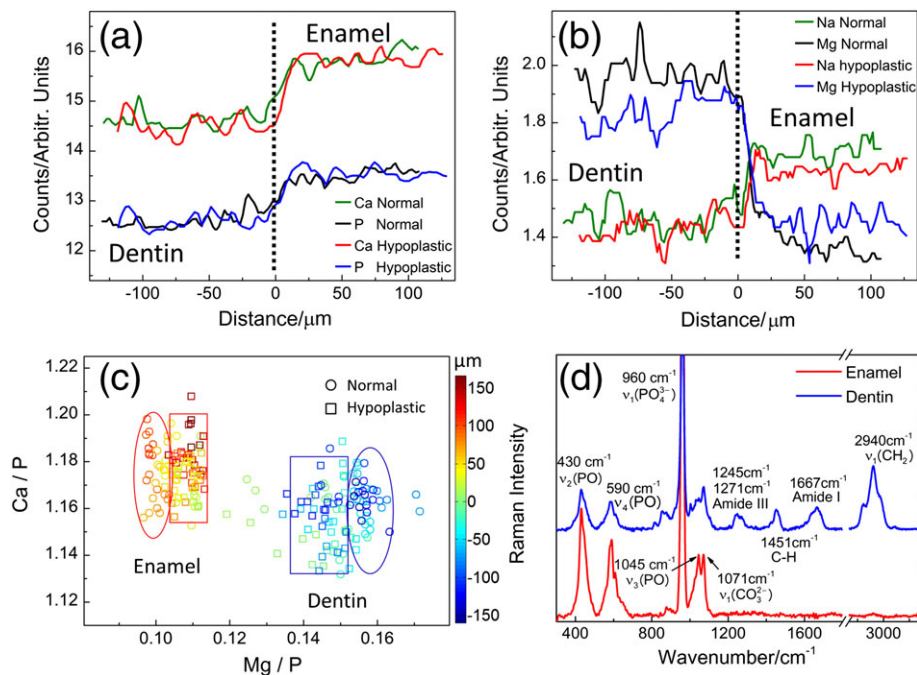
FIGURE 2 Relative distribution of main element Ca and P of the normal and hypoplastic tooth (a). Relative amounts of trace element Na and Mg of normal and hypoplastic tooth (b). Correlation of ratios of Ca/P and Mg/P (c), where false color scale indicates the measurement position from dentin to enamel relative to the dentin–enamel junction. Representative baseline corrected Raman spectra of dental enamel and dentin (d) [Colour figure can be viewed at wileyonlinelibrary.com]

3.3 | Spatio-spectral imaging across the DEJ

We then perform spatio-spectral imaging with high spatial resolution across the DEJ at both the occlusal and cervical positions for normal and hypoplastic tooth, respectively. We extract integral intensity and linewidth (FWHM) by peak fitting at each image pixel. The integral intensity of the 960 cm^{-1} band indicates the phosphate content, and the linewidth serves as a measure of hydroxyapatite crystal-chemical characteristics (substitution/crystallographic parameter).

Figure 3 shows the corresponding results for the totally symmetric P-O band stretch at 960 cm^{-1}. Figure 3a–d shows the results for normal tooth, in which (a) and (b) are the intensity images, and (c) and (d) the corresponding linewidth images. Figure 3e–h shows the corresponding results for the hypoplastic tooth. For all images, the intensity in the enamel is larger than in dentin, whereas the linewidth is larger in dentin than in enamel, yet with characteristic spatial variations.

At occlusal position, Figure 3a,e, the elongated structural features in the enamel near the DEJ (black arrows) are the enamel spindles, which are remnants from the initial enamel development. The intensity is lower at the enamel spindle because of the reduced inorganic mineral content, yet with no discernible change in spectral width. At the cervical position, where the enamel development is later than at the occlusal position, there is little spindle structure in enamel.

For the hypoplastic tooth, Figure 3e,f, the intensity distribution of the P-O stretch is similar between the normal and hypoplastic teeth within about 40 μm range near the junction. The intensity of the P-O stretch in the hypoplastic tooth decreases again in the enamel further away from the DEJ, due to a higher organic content, whereas the P-O intensity remains high throughout the enamel in the normal tooth. However, most notably, little decrease in FWHM of the P-O stretch is seen in the hypoplastic enamel along either the cervical or occlusal directions with distance away from the DEJ, as further investigated below.

3.4 | Hyper-spectral Raman imaging

In order to investigate local variations associated with structural variations of ID as the bulk dentin, DT, DEJ, and enamel, we perform micro-Raman with high throughput and enhanced spectral precision in cervical locations, as shown in Figure 4 for the healthy tooth as example, acquired over a 20 μm × 200 μm area across the DEJ, with 0.5-μm step sizes, spectra acquired for 3.5 s each, for a total scan time of 16 hr for 16,000 spectra.
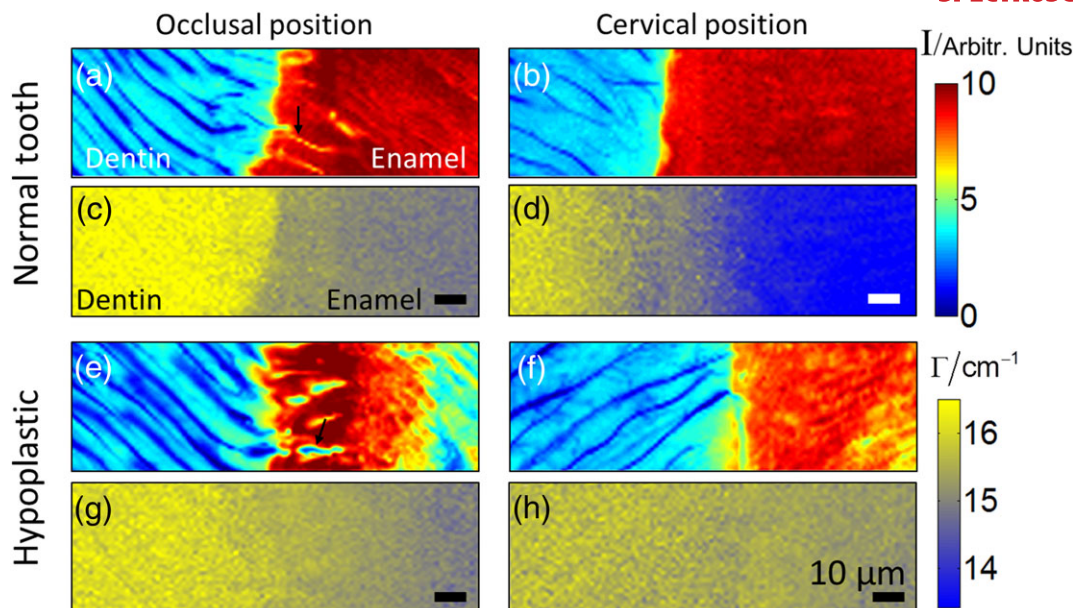
FIGURE 3   Raman mapping with integral intensity and linewidth of the 960 cm^{-1} P-O stretch mode across the dentin–enamel junction of normal (a–d) and hypoplastic (e–h) tooth. Image size is 110 μm by 40 μm with 1 μm step size. (a), (b), (e), and (f) are intensity images whereas (c), (d), (g), and (h) are linewidth images [Colour figure can be viewed at wileyonlinelibrary.com]
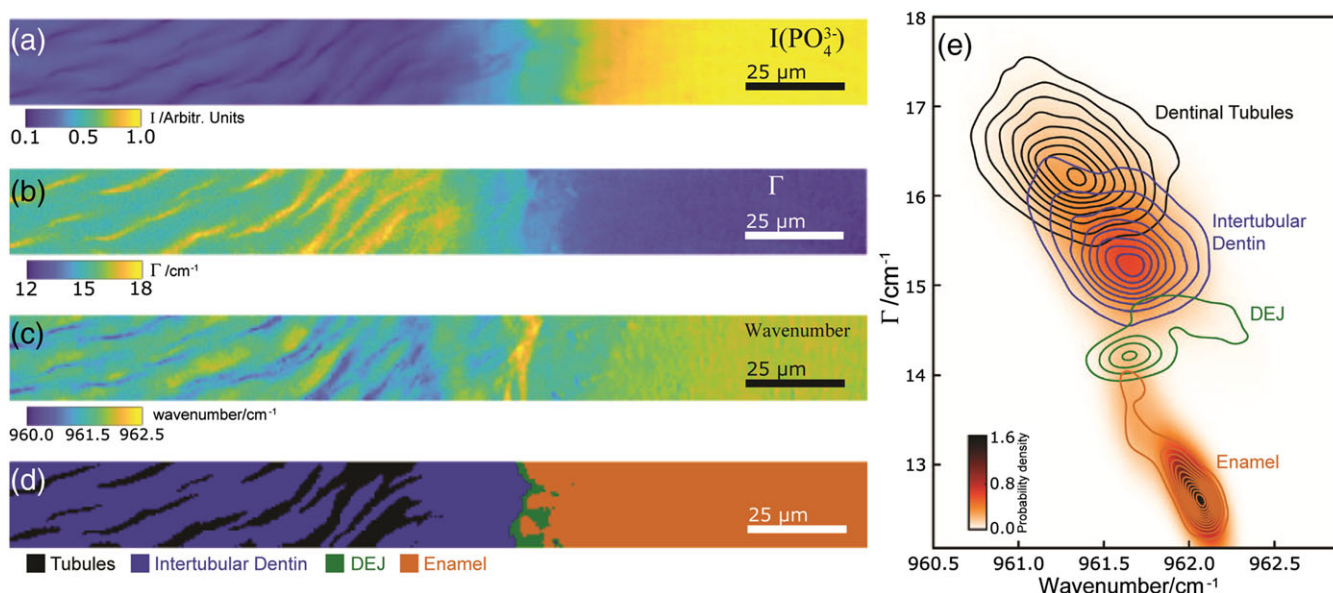
FIGURE 4   High throughput high precision hyper-spectral Raman imaging of the totally symmetric 960 cm^{-1} P-O stretch mode with computational lineshape analysis with images of intensity (a), FWHM (b), and spectral position (c). By setting different thresholds in intensity (d), four distinct populations can be discerned representing dentinal tubules, intertubular dentin, DEJ interface region, and bulk enamel. Corresponding plot of FWHM vs. linewidth (e) highlights their distinct characteristics, yet their well-correlated behavior indicates a common mechanism of static disorder across all four regions. DEJ: dentin–enamel junction; FWHM: full width at half maximum [Colour figure can be viewed at wileyonlinelibrary.com]

Figure 4a–c shows images of peak intensity I, linewidth Γ, and spectral position ν, respectively, obtained from computational spatio-spectral Voigt profile peak analysis. As can be seen and extending the lower resolution fast scan imaging above (Figure 3), distinct variations both in peak position and linewidth can now

be discerned and correlated with the characteristic structural features within dentin and enamel. Already qualitatively, the DT exhibit the highest FWHM values, followed by the ID, the DEJ interfacial region, and the bulk enamel with the lowest values, and correlated with small variations in peak position from the highest values in the

bulk enamel to the lowest frequencies in the DT. From a cluster analysis, by setting appropriate threshold values in intensity, these four distinct regions can clearly be separated and identified (Figure 4d). The DEJ and enamel thresholds were selected based on a clear dentin–enamel delineation identified by the transition in protein content from the amide I Raman image (for data, see Figure S3). The dental tubule and lower ID intensity threshold value was chosen such that a 0.05 increase in the value would encapsulate more than 50% of the total dentin as tubule, whereas a 0.05 decrease would give rise to over 97% of the dentin being classified as intertubule. From the corresponding plot of FWHM versus peak position (Figure 4e) from the data in (Figure 4b–c), the regions of tubules, ID, DEJ, and enamel can be discerned by distinct centroids in Γ-ν distributions with only small statistical overlap. The distributions in Figure 4e were generated using a Gaussian kernel density estimator to arrive at a probability density function for each population (underlying scatter plot, see Figure S4). Here, the enamel stands out with a narrow distribution of lineshapes, with a small subset of the population elongated towards higher linewidth and corresponding red shift, which corresponds to the enamel closer to the DEJ. A qualitatively different behavior then starts at the DEJ with a substantial spread in wavenumber. While continuing the correlated trend of spectral broadening from the DEJ, via ID to the DT region, the responses in these regions are characterized by substantial inhomogeneous broadening, with no obvious spatial correlation within these regions. However, the overall well-correlated behavior of continuous broadening (increase in FWHM) with systematic P-O bond softening (red shift) across all clusters suggests a common mechanism of static crystalline disorder through substitution and corresponding crystal lattice change both in dentin and enamel as discussed below.

3.5 | Long-range variation in crystallinity

In order to investigate changes in crystallinity across the enamel, we measure linewidth on the mm scale along a trajectory across the enamel and along the outer tooth surface as indicated in inset of Figure 5.

Figure 5 shows the resulting FWHM across enamel from inside dentin (left, −0.5 mm) to the outer enamel surface (right, 2.0 mm). In the dentin region, the FWHM of normal and hypoplastic tooth is largely homogeneous on the 100's μm scale, yet with a slightly lower linewidth in the hypoplastic tooth. In contrast, in the enamel region, the FWHM decreases continuously from ~14.5 cm^{-1} to as low as 11 cm^{-1} at the outer tooth surface, reaching similar values for the FWHM at the tooth surface (Figure 5, the deep blue dots) yet at different rates
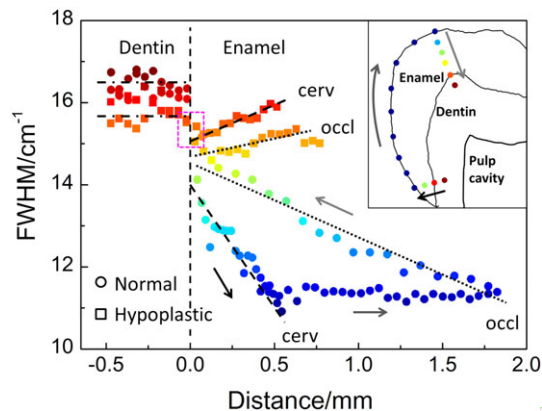
FIGURE 5 FWHM of 960 cm^{-1} mode along the path from the DEJ at cervical position (black arrow) to tooth surface (light black arrow) and back to DEJ at occlusal position (grey arrow). Inset: schematic of tooth segment to show the measurement path. Cerv and occl are the abbreviation of cervical and occlusal position. Pink box indicates detailed FWHM variations near DEJ (see Figure S5). DEJ: dentin–enamel junction; FWHM: full width at half maximum [Colour figure can be viewed at wileyonlinelibrary.com]

as a function of distance. Thus, the FWHM of normal enamel not only varies at the DEJ but also along the full range of enamel.

In contrast, the FWHM of the hypoplastic tooth does not decrease with distance from the DEJ. The FWHM rather varies between 14.5 and 16 cm^{-1} and tends to increase with distance from the DEJ towards the outer tooth surface.

4 | DISCUSSION

The results above show the sensitivity of the ν_1 PO$_4^{3-}$ P-O stretch mode as a probe of the heterogeneity in the local chemical environment due to ionic substitution, local disorder, and organic content from the μm scale to the macroscale.

A well-established characteristic is the sharp transition of the Raman response between enamel and dentin at the DEJ[9–11] over a transition length of as short as few to several 10's μm, most pronounced in the difference in the intensity of the protein versus inorganic Raman response and the associated change in line width of the 960 cm^{-1} mode.

A new qualitative characteristic is the distinct difference in the enamel response between healthy and hypoplastic tooth. A largely constant FWHM in dentin and enamel of the hypoplastic tooth contrasts a divergence in the FWHM between the enamel versus dentin in normal teeth. Recent studies of amelogenesis imperfecta teeth[7,8,25–27,30] identified low degree of crystallinity at

selected locations and linked to higher carbonate content in the hypomineralized/hypoplastic enamel. However, in our hypoplastic case, the signature of an elevated protein content in hypoplastic enamel (see Figure S6) with only a minor difference in Ca/P, too small to account for the Raman spectral differences, would rather suggest the protein content as the origin of the reduced degree of mineralization and crystallinity.[7,25,27] It is worth noting that not all tooth disorders lead to a decreased linewidth. Low values of FWHM in a study of sclerotic dentin in noncarious cervical lesions[12,13] suggested a hypermineralized dentin in that case. Similarly, an increase in fluorine content leads to an increase in apatite density and decrease in solubility, based on an increase in crystallinity and reduced linewidth.[32]

Attempts have been made to relate the FWHM as a metric for crystallinity[7,9,16,17,33,34], however, because of the indirect sensitivity of the Raman response, especially in biological matter, this proves difficult to relate to specific structural changes, disorder, ionic substitutions, or sample heterogeneity or a combination of these effects. However, this situation can be improved with (a) the increased spatio-spectral content, notably the Γ-ν correlation obtained in this work, and (b) from direct comparison with elemental composition obtained and novel structural knowledge about the crystal chemistry of hydroxyapatite in recent work from the application of spatially resolved X-ray and electron-based structural imaging probes.[20,26,29,35]

In general, the spectral broadening of the 960 cm^{-1} mode in dentin compared with enamel can be attributed to the carbonate substitution for PO_4^{3-} (B type) ions involving the formation of a Ca^{2+} and an OH^- vacancy.[36–38] This substitution is believed to lead to a loss of long-range structural order, and the resulting inhomogeneity gives rise to spectral broadening. This B-type carbonate substitution for PO_4^{3-} with associated vacancy formation and lattice distortion only leads to a comparably small spectral shift.[36,37] However, the combination with the minor A-type substitution (B:A $\approx$9:1[4,8]) can then account for the observed correlated variation in Γ and ν due to structural disorder associated with the substitution as has been shown in several geological and biomineral apatite systems.[12,32,33,39]

As seen in Figure 4, the bulk phase of the enamel is characterized by the highest mode frequencies, low FWHM values, and with a narrow distribution in Γ-ν. Although the Raman spectral behavior can not a priori be related to chemical substitution or crystal structure parameters, our work demonstrated how the ν_1 PO_4^{3-} mode is sensitive to ionic substitution on neighboring lattice sites, which gives rise to a decreasing structural order and spectral broadening.[35,39,40] Starting at the DEJ interface

region, the enamel exhibits a red shift and broadening within a comparatively narrow Γ-ν distribution, yet with a tail towards a much broader wavenumber distribution. These transitions into the ID with considerable broadening are most likely driven by ionic substitution induced disorder. Further red shift in the DT phase, with large broadening, is likely due to further disorder induced by the protein content. This latter interpretation is supported by the study of the crystallinity locally near the DEJ at the occlusal position where a correlation of phosphate content with collagen crosslinking has been found.[9]

The continuous long range decrease of Mg^{2+}, Na^+, and CO_3^{2-} content and correlated increase in Ca^{2+} and PO_4^{3-} across the enamel from the DEJ to the outer enamel surface[16,18,20,29,30] then also explains the observed spectral narrowing through increased crystallinity. Our results suggest that irrespective of enamel thickness and location, the crystallinity converges to similar degrees across the entire tooth surface. Considering the almost pure hydroxyapatite at the tooth surface, the enhanced crystallinity is associated with the larger size and order of the nanocrystallites.[20] This result agrees with imaging of the hardness and elastic modulus.[18]

Recent micro X-ray diffraction and synchrotron studies have identified the relationship of the spatio-chemical distribution with associated changes in lattice parameter and structural order/disorder. Mg^{2+} plays an important role as doped ion to influence the crystal cell parameters.[18,20,29] Dentin crystallite lattices were found to be much more disordered with limited size and microstrain than enamel.[41] A continuous increase in the a-lattice parameter (apatite space group $P6_3/m$) was found from the DEJ to the outer enamel surface associated with an increase in crystallite size and alignment.[19,20,41,42] From comparison of X-ray diffraction tomography with elemental EDX mapping that increase in a-lattice parameter is most likely caused by Mg^{2+} substitution on the Ca^{2+} site.[20]

5 | CONCLUSION

Our results show heterogeneity in Raman response on multiple length scales characterizing spatio-chemical and structural variations in normal and disease disordered tooth. We established the systematic relationship of elemental distribution associated changes in crystallinity and their manifestation in the linewidth and spectral position of phosphate Raman mode as sensitive reporter of the local chemical and structural environment. Our results thus present a means for additional chemical

and structurally sensitive imaging complementary to established methods and opening a route towards greater understanding from geologic and biogenic apatite systems.

DISCLOSURES

The authors declare no conflicts of interest.

ORCID

Markus B. Raschke 🔟 http://orcid.org/0000-0003-2822-851X

REFERENCES

[1] Z. Movasaghi, S. Rehman, D. I. U. Rehman, *Appl. Spectrosc. Rev.* **2007**, *42*, 493.

[2] A. Carden, M. D. Morris, *J. Biomed. Opt.* **2000**, *5*, 259.

[3] R. Ramakrishnaiah, G. Rehman, S. Basavarajappa, A. A. A. Khuraif, B. H. Durgesh, A. S. Khan, I. Rehman, *Appl. Spectrosc. Rev.* **2015**, *50*, 332.

[4] P. G. Spizzirri, N. J. Cochrane, S. Prawer, E. C. Reynolds, *Caries Res.* **2012**, *46*, 353.

[5] A. C. T. Ko, L. P. C. Smith, M. Hewko, M. G. Sowa, C. C. S. Dong, B. Cleghorn, *Opt. Express* **2006**, *14*, 203.

[6] P. Seredin, D. Goloshchapov, T. Prutskij, Y. Ippolitov, *Plos One* **2015**, *10*, 0124008.

[7] Y. Sa, S. Liang, X. Ma, S. Lu, Z. Wang, T. Jiang, Y. Wang, *Acta Biomater.* **2014**, *10*, 5169.

[8] F. Taube, M. Marczewskib, J. G. Norén, *J. Dent.* **2015**, *43*, 269.

[9] A. Slimani, F. Nouioua, A. Desoutter, B. Levallois, F. J. G. Cuisinier, H. Tassery, E. Terrer, H. Salehi, *J. Biomed. Opt.* **2017**, *22*, 086003.

[10] M. A. Alebrahim, C. Krafft, J. Popp, *Mater. Sci. Eng.* **2015**, *92*, 012014.

[11] C. Xu, X. Yao, M. P. Walker, Y. Wang, *Calcif. Tissue Int.* **2009**, *84*, 221.

[12] C. Xu, K. Karan, X. Yao, Y. Wang, *J. Raman Spectrosc.* **2009**, *40*, 1780.

[13] K. Karan, X. Yao, C. Xu, Y. Wang, *Dent. Mater.* **2009**, *25*, 1205.

[14] Z. Wang, W. Zheng, C. Y. S. Hsu, Z. Huang, *Appl. Phys. Lett.* **2016**, *108*, 348.

[15] S. Yang, B. Li, A. Akkus, O. Akkus, L. Lang, *Analyst* **2014**, *139*, 3107.

[16] C. Xu, R. Reed, J. P. Gorski, Y. Wang, M. P. Walker, *J. Mater. Sci.* **2012**, *47*, 8035.

[17] Y. Sa, Y. Guo, X. Feng, M. Wang, P. Li, Y. Gao, X. Yang, T. Jiang, *New J. Chem.* **2017**, *41*, 5723.

[18] J. L. Cuy, A. B. Mann, K. J. Livi, M. F. Teaford, T. P. Weihs, *Arch. Oral Biol.* **2002**, *47*, 281.

[19] M. A. Jawada, A. Steuwer, S. H. Kilcoyne, R. C. Shore, R. Cywinski, D. J. Wood, *Biomaterials* **2007**, *28*, 2908.

[20] C. K. Egan, S. D. M. Jacques, M. D. Michiel, B. Cai, M. W. Zandbergen, P. D. Lee, A. M. Beale, R. J. Cernik, *Acta Biomater.* **2013**, *9*, 8337.

[21] T. Cloitre, I. V. Panayotov, H. Tassery, C. Gergely, B. Levallois, F. J. G. Cuisinier, *J. Biophotonics* **2013**, *6*, 330.

[22] S. Amarie, P. Zaslansky, Y. Kajihara, E. Griesshaber, W. W. Schmahl, F. Keilmann, *Beilstein J. Nanotechnol.* **2012**, *3*, 312.

[23] M. Schirmer, M. Fujio, M. Minami, J. Miura, T. Araki, T. Yasui, *Biomed. Opt. Express* **2010**, *1*, 354.

[24] M. J. Aldred, R. Savarirayan, P. Crawford, *Oral Dis.* **2003**, *9*, 19.

[25] P. Qing, Y. Li, S. Gao, M. Qiao, L. Qian, H. Yu, *Adv. Mech. Eng.* **2015**, *7*, 1.

[26] S. J. Fraser, A. K. Natarajan, A. S. S. Clark, B. K. Drummond, K. C. Gordon, *J. Raman Spectrosc.* **2015**, *46*, 202.

[27] A. K. Natarajan, S. J. Fraser, M. V. Swain, B. K. Drummond, K. C. Gordon, *Anal. Bioanal. Chem.* **2015**, *407*, 5661.

[28] J. P. Simmer, P. Papagerakis, C. E. Smith, D. C. Fisher, A. N. Rountrey, L. Zheng, J. C. C. Hu, *J. Dent. Res.* **2010**, *89*, 1024.

[29] V. Srot, B. Bussmann, U. Salzberger, C. T. Koch, P. A. Aken, *Microsc. Microanal.* **2012**, *18*, 509.

[30] L. Melin, J. Lundgren, P. Malmberg, J. G. Norén, F. Taube, D. H. Cornell, *Microsc. Microanal.* **2015**, *21*, 407.

[31] M. T. Kirchner, H. G. M. Edwards, D. Lucy, A. M. Pollard, *J. Raman Spectrosc.* **1997**, *28*, 171.

[32] J. J. Freeman, B. Wopenka, M. J. Silva, J. D. Pasteris, *Calcif. Tissue Int.* **2001**, *68*, 156.

[33] E. Pucéat, B. Reynard, C. Lécuyer, *Chem. Geology.* **2004**, *205*, 83.

[34] G. S. Mandair, M. D. Morris, *Bonekey Rep.* **2015**, *4*, 620.

[35] D. B. Thomas, C. M. McGoverin, R. E. Fordyce, R. D. Frew, K. C. Gordon, *Palaeogeogr. Palaeocl.* **2011**, *310*, 62.

[36] G. Penel, G. Leroy, C. Rey, E. Bres, *Calcif. Tissue Int.* **1998**, *63*, 475.

[37] F. F. M. Mul, C. Otto, J. Greve, J. Arends, J. J. Bosch, *J. Raman Spectrosc.* **1988**, *19*, 13.

[38] R. Z. Legeros, O. R. Trautz, J. P. Legeros, E. Klein, W. P. Shirra, *Science* **1967**, *155*, 1409.

[39] L. Zhang, L. Cao, L. Zhao, T. J. Algeo, Z. Q. Chen, Z. Li, Z. Lv, X. Wang, *Geochim. Cosmochim. Ac.* **2017**, *210*, 184.

[40] D. B. Thomas, R. E. Fordyce, R. D. Frew, K. C. Gordon, *J. Raman Spectrosc.* **2007**, *38*, 1533.

[41] P. Zioupos, K. D. Rogers, *J. Bionic Eng.* **2006**, *3*, 019.

[42] J. Xue, A. V. Zavgorodniy, B. J. Kennedy, M. V. Swain, W. Li, *J. Microsc.* **2013**, *251*, 144.

SUPPORTING INFORMATION

Additional supporting information may be found online in the Supporting Information section at the end of the article.